

Supplementary Materials for

An ocular glymphatic clearance system removes β -amyloid from the rodent eye

Xiaowei Wang, Nanhong Lou, Allison Eberhardt, Yujia Yang, Peter Kusk, Qiwu Xu, Benjamin Förster, Sisi Peng, Meng Shi, Antonio Ladrón-de-Guevara, Christine Delle, Björn Sigurdsson, Anna L. R. Xavier, Ali Ertürk, Richard T. Libby, Lu Chen*, Alexander S. Thrane, Maiken Nedergaard*

*Corresponding author. Email: nedergaard@sund.ku.dk (M.N.); chenlu@berkeley.edu (L.C.)

Published 25 March 2020, *Sci. Transl. Med.* **12**, eaaw3210 (2020)

DOI: 10.1126/scitranslmed.aaw3210

The PDF file includes:

Fig. S1. Characterization of additional tracers and tracer delivery routes.

Fig. S2. Brief retinal exposure to trace amounts of hA β using our intravitreal infusion paradigm does not induce gliosis, microglial activation, apoptosis or BRB disruption.

Fig. S3. Detailed analysis of ocular glymphatic clearance route.

Fig. S4. Validation of tracer delivery model in another species and with different infusion parameters.

Fig. S5. Light stimulation accelerates hA β tracer movement along the optic nerve.

Fig. S6. Influence of the translaminal pressure difference on stimulated and unstimulated tracer movement.

Fig. S7. Tracer efflux pattern in murine glaucoma model indicates leaky lamina that may allow bypass of intra-axonal transport via extracellular route.

Fig. S8. Murine glaucoma models reveal defects in the lamina barrier allowing escape of large intraocular tracers.

Fig. S9. Schematic model of the ocular glymphatic clearance system and its dysfunction in a murine model of glaucoma.

Table S1. Retinal cytokine assay comparing intravitreal hA β injection to vehicle.

Table S2. Comparison of the controls for the DBA/2J strain.

Table S3. Tracers used and their routes of administration.

Legend for movie S1

Other Supplementary Material for this manuscript includes the following:

(available at stm.sciencemag.org/cgi/content/full/12/536/eaaw3210/DC1)

Movie S1 (.mov format). Animation of the proposed mechanism for ocular glymphatic clearance in the healthy optic nerve and glaucoma.

Data file S1. Tabular summary of all the data (provided as separate excel file).

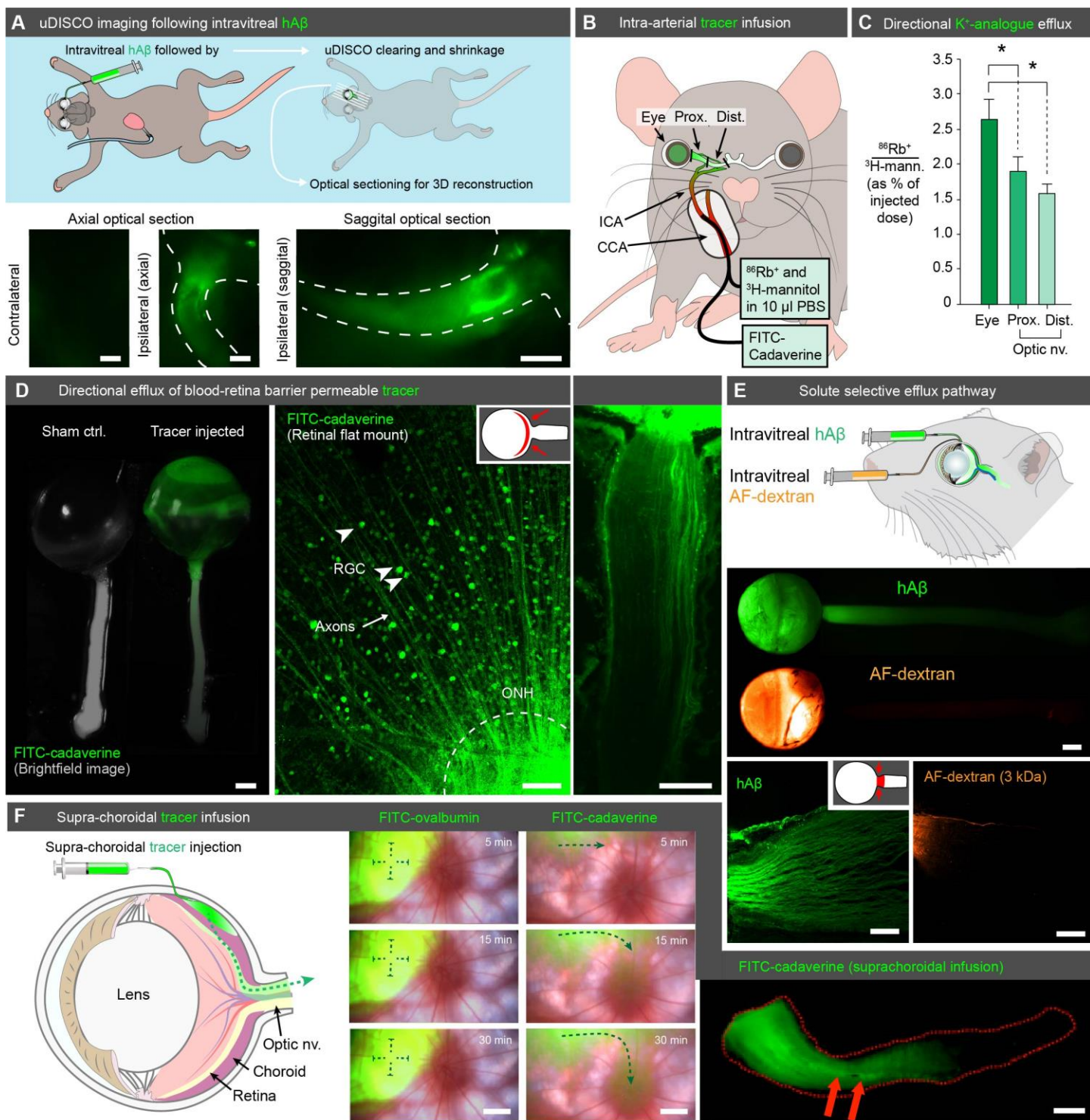


Fig. S1. Characterization of additional tracers and tracer delivery routes. (A) Top: Schematic showing hA β injection followed by uDISCO whole-mouse clearing and shrinkage, along with optical sectioning using light sheet microscopy. Bottom: Representative maximum projections acquired in axial and sagittal plane

ipsilateral and contralateral to the hA β injection (scale: 500 μ m). **(B)** Schematic showing non-invasive tracer delivery via injection into the internal carotid artery (ICA). **(C)** Quantification of $^{86}\text{Rb}^+ / ^3\text{H}$ -mannitol radioactivity in the ipsilateral eye and optic nerve following ICA injection shows directional flow of the K $^+$ -analogue from the eye to the optic nerve ($n = 7$, $*p < 0.05$, one-way ANOVA followed by Dunnett's *post hoc* test). **(D)** Left: Macroscopic imaging following FITC-cadaverine ICA injection showing ipsilateral eye and optic nerve (right) compared to that from a naïve mouse (left). FITC signal (green) is superimposed on bright field (scale: 1 mm). Middle: Confocal image of the mouse retina following ICA injection of FITC-cadaverine. Arrowhead pointing to retinal ganglion cells (RGC) up taking of the tracer. Arrow pointing to RGC axons taking up the blood-retina-barrier-permeable tracer. Right: Confocal image of mouse optic nerve following intravitreal administration of FITC-cadaverine (scale: 100 μ m). **(E)** Fluorescent macroscopic (scale: 500 μ m) or confocal images (scale: 100 μ m) of the eye and optic nerve following intravitreal injection of either the axon-transportable tracer hA β or the non-transportable tracer AF-dextran (3 kDa). **(F)** Left: Schematic of suprachoroidal tracer delivery and tracer movement. Middle: Representative funduscopy images following suprachoroidal FITC-ovalbumin or FITC-cadaverine (scale: 300 μ m). Green arrow indicates the direction of FITC-cadaverine movement. Right: Representative confocal image of ipsilateral optic nerve following suprachoroidal FITC-cadaverine injection (scale: 500 μ m). Red arrow points to central retinal vein.

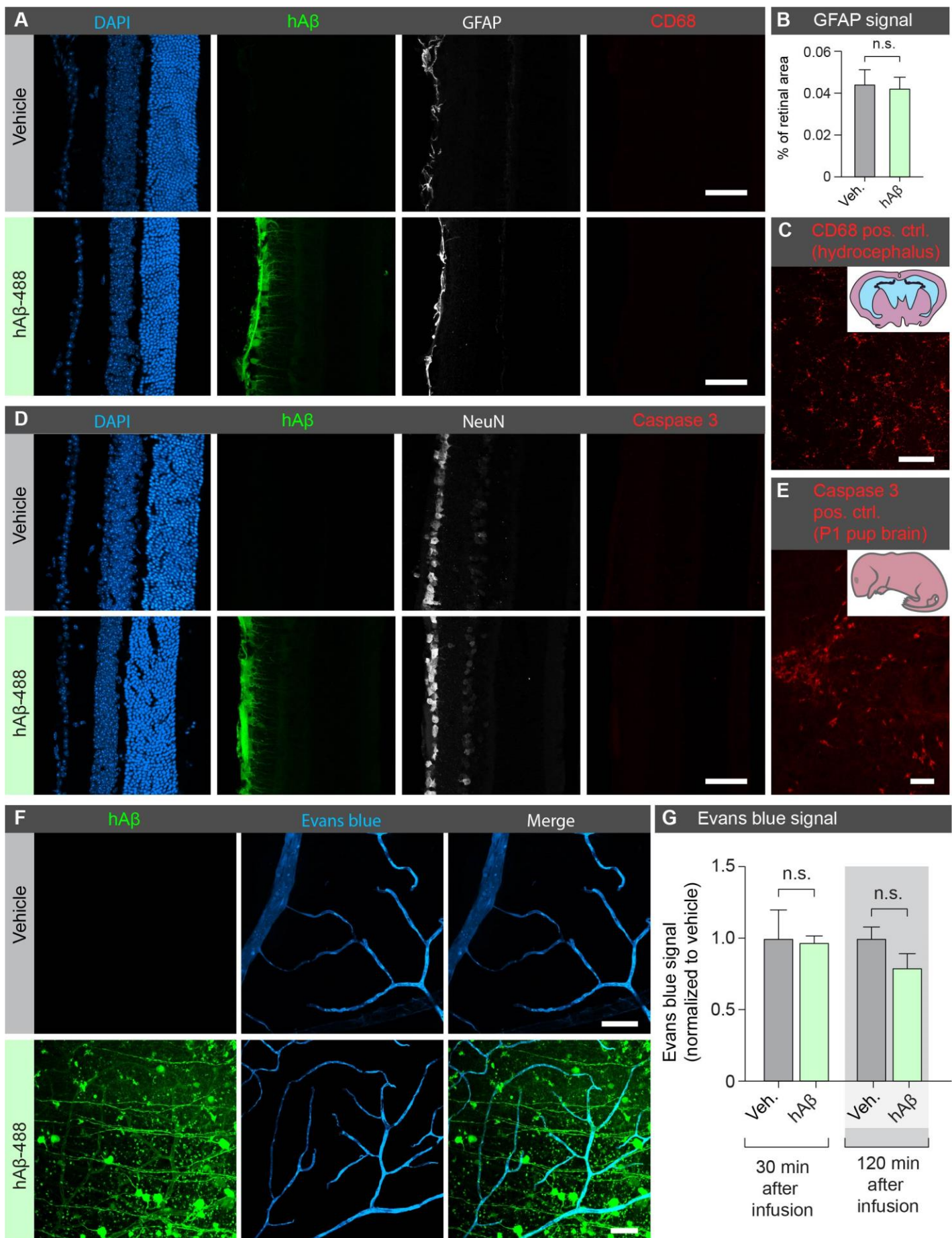


Fig. S2. Brief retinal exposure to trace amounts of hA β using our intravitreal infusion paradigm does not induce gliosis, microglial activation, apoptosis or BRB disruption. (A) Representative confocal transverse retinal sections following intravitreal injection of vehicle or hA β (green) counterstained for glial fibrillary acidic protein (GFAP, white) and microglial marker CD68 (red). (B) Quantification of percentage retinal area positive for GFAP ($n = 9-11$, n.s. $p = 0.656$, Mann-Whitney test). (C) Positive control (pos. ctrl.) for CD68 (8-week-old hydrocephalic mouse neocortex). (D) Representative confocal transverse retinal sections following intravitreal injection of vehicle or hA β counterstained for neuronal marker NeuN (white) and apoptosis marker caspase 3 (red). (E) Positive control for caspase 3 (P1 mouse pup brain). (F) Representative confocal flat-mount retinal images following intravascular Evans blue and intravitreal hA β (green) or vehicle administration. (G) Quantification of Evans blue signal normalized to vehicle at different time points after intravitreal administration of hA β vs. vehicle ($n = 3-4$, n.s. $p = 0.858$ for 30 min and $p = 0.268$ for 120 min, paired t -test). (Scale: A, C, D, E, F: 50 μ m).

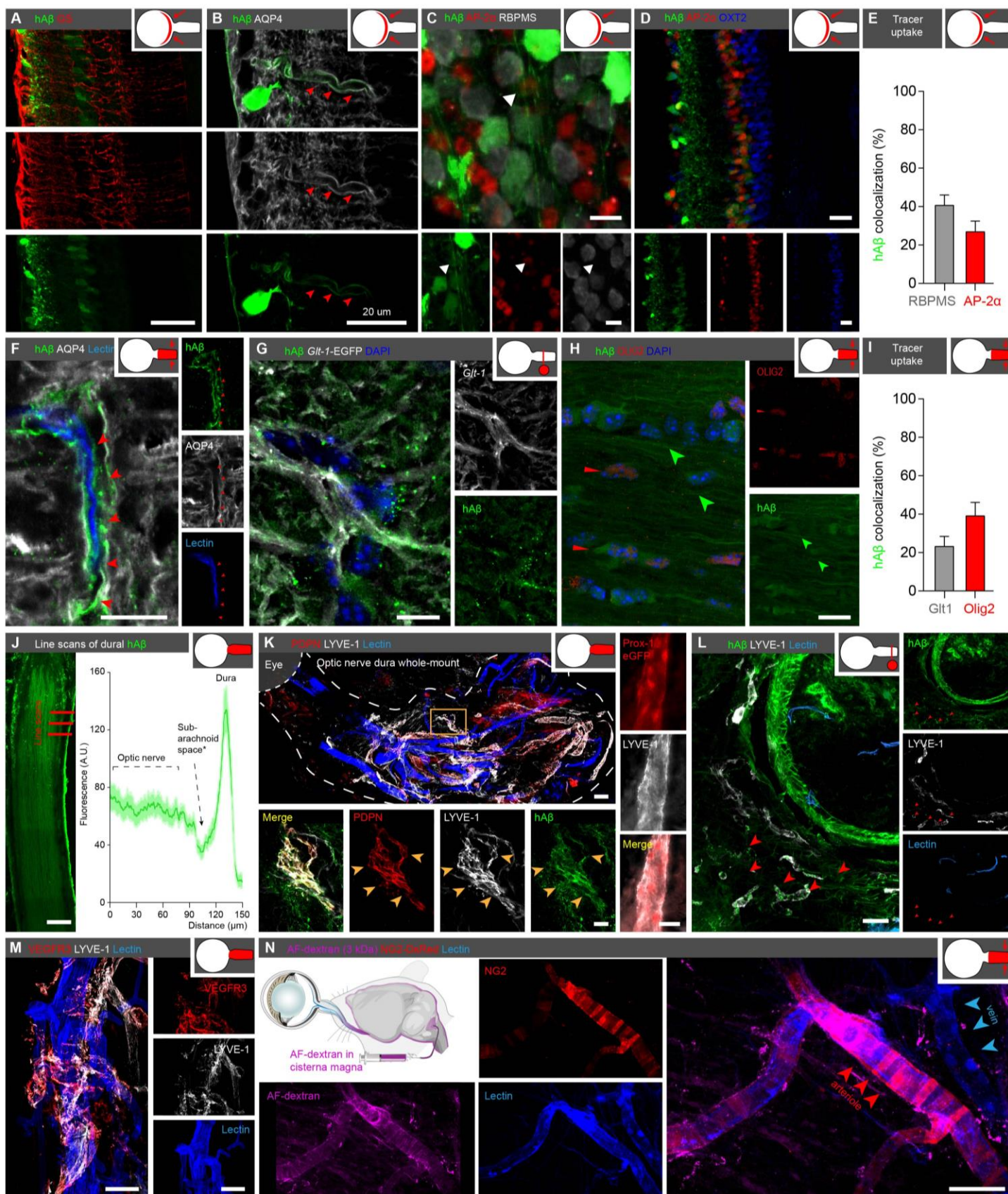


Fig. S3. Detailed analysis of ocular glymphatic clearance route. (A) Confocal images of mouse retina counter-stained for glutamine synthetase (GS, scale: 50 μm). (B-D) Confocal image of mouse retina counter-stained for aquaporin-4 (AQP4), AP-2 α , RNA-binding protein with multiple splicing (RBPMS), and orthodenticle homeobox-2 (OXT2). Red arrowheads point to perivascular space outlined by AQP4⁺ glial endfeet. White arrowheads point to uptake by AP-2 α ⁺ cells. (E) Percentage of retinal cellular uptake (mean \pm SEM, n = 7). All images are retinal cross-sections except C, which is a retinal flat-mount image (scale: 20 μm). (F) Confocal image of hA β tracer distribution in optic nerve counter stained with AQP4. Red arrowheads point AQP4-outlined perivascular (scale: 10 μm). (G) Confocal images of hA β tracer distribution in GLT1-eGFP⁺ optic nerve after intravitreal injection (scale: 10 μm). (H) Confocal images of hA β tracer distribution in optic nerve counter stained with Oligodendrocyte transcription factor (OLIG2). Red arrowheads indicate hA β signal in OLIG2⁺ soma; green arrowheads indicate hA β signal in axons (scale: 10 μm). (I) Percentage of glial uptake in the optic nerve (mean \pm SEM, n = 4-12). (J) Left: Representative photo-stitched longitudinal section illustrating 150 μm line-scans at the interface of optic nerve and dura. Right: Line graph showing fluorescence intensity (mean \pm SEM) of 20 line scans collected from 4 mice 300-900 μm posterior to the glial lamina. (scale: 100 μm). (K) Left: Whole-mount of dura stripped from the optic nerve following intravitreal hA β . Yellow arrowheads points to LYVE1⁺, PDPN⁺, and hA β ⁺ vessel-like structures (scale: 100 μm in top image, 20 μm in bottom images). Right: Optic nerve dura mater whole-mount immunostaining of LYVE1- and PROX1- positive lymphatics in *Prox1*-GFP mouse (Images were presented in pseudo colors) (scale: 20 μm). (L) Immuno-detection of LYVE1 in cross-section of optic nerve following hA β tracer intravitreal injection. Red arrowheads points to hA β tracer uptake by LYVE1⁺, intravascular lectin-negative structures in the dura and orbital tissue surrounding the optic nerve (scale: 20 μm). (M) Dural whole-mount showing LYVE1⁺ and VEGFR3⁺ structures, devoid of intravascular lectin (scale: 100 μm). (N) Confocal images of the optic nerve from an NG2-DsRed mouse following cisterna magna (CM) injection. Red arrowheads point to periarterial space; blue arrowheads point to perivenous space (scale: 50 μm).

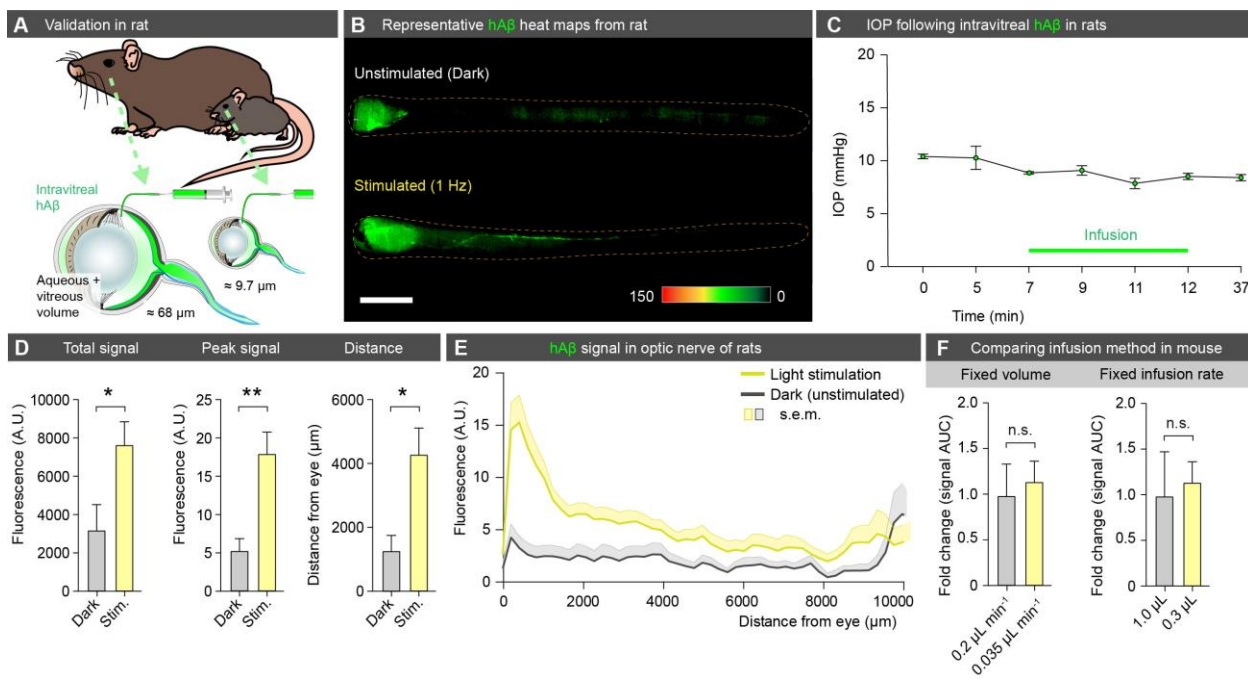


Fig. S4. Validation of tracer delivery model in another species and with different infusion parameters. (A) Schematic showing intravitreal hAβ infusion in Brown Norway rat, which has approximately seven times the intraocular fluid volume of a C57BL/6J mouse. (B) Representative background-subtracted heat-maps from rats kept in darkness or subjected to 1 Hz light stimulation following intravitreal hAβ infusion (scale: 1 mm). (C) IOP measured by rebound tonometry during the hAβ infusion in rats ($n = 3$). (D) Total hAβ signal, peak hAβ signal, and distance travelled for unstimulated and stimulated (1 Hz) rat eyes ($n = 5-7$, $*p < 0.05$, $**p < 0.01$, unpaired two-tailed t -test). (E) Averaged fluorescent intensity profile of hAβ tracer distribution along rat optic nerve ($n = 5-7$). (F) The impact of hAβ infusion volume and rate on overall optic nerve signal (AUC = area under the curve) were compared in mouse ($n = 6-11$, n.s. $p = 0.462$ for fixed volume and $p = 0.366$ for fixed rate, Mann-Whitney test).

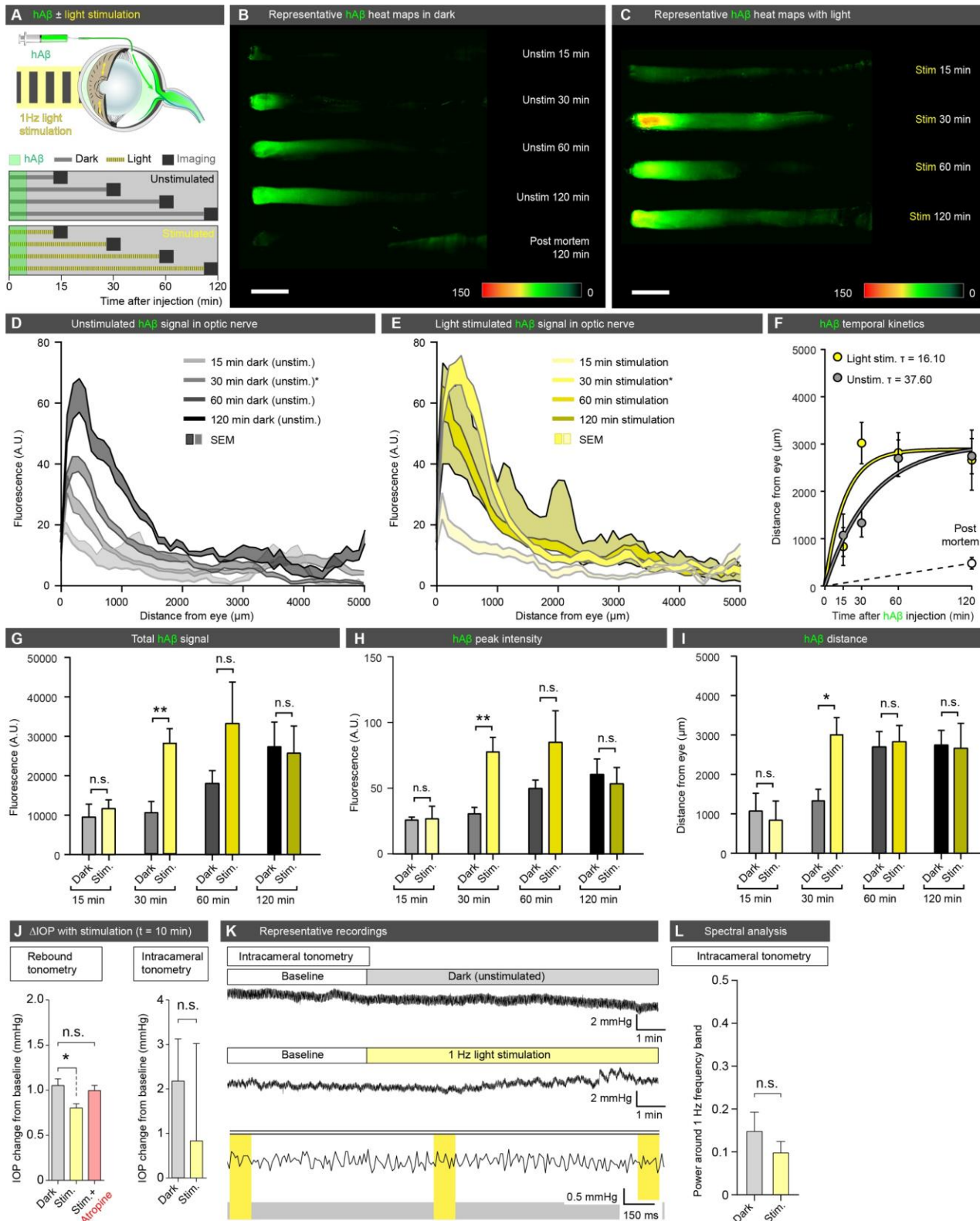


Fig. S5. Light stimulation accelerates hAβ tracer movement along the optic nerve. (A) Schematic of experiment design. Mice were subjected to either dark or 1 Hz light stimulation (100 ms duration, 5 lumens)

and imaged 15, 30, 60, or 120 min after intravitreal hA β injection. **(B-C)** Representative background-subtracted heat-maps of optic nerves following hA β tracer injection in all experiment groups and postmortem group (scale: 1 mm). **(D-E)** Averaged fluorescent intensity profiles of hA β tracer distribution along the optic nerve in dark, unstimulated and light-stimulated groups at 15-, 30-, 60-, and 120-minute time points ($n = 3-8$). **(F)** Pseudo-kinetics of the hA β tracer movement shown by fitting the distance and experiment time to a one-phase decay curve ($n = 3-8$). **(G-I)** Total hA β tracer signal, peak intensity, and distance travelled in the optic nerve for all the groups. ($n = 3-8$, $*p < 0.05$, $**p < 0.01$, n.s. $p = 0.193-0.946$, unpaired two-tailed t -test). **(J)** Left: Comparison of the relative change of IOP in light-stimulated (\pm atropine) vs. control (dark) groups using rebound tonometry ($n = 14-15$ for each group, $*p < 0.05$, n.s. $p = 0.6973$, one-way ANOVA followed by Dunnett's *post hoc* test) measured 10 min after starting the experiments normalized to IOP baseline. Right: Intracameral tonometry ($n = 5-6$, n.s. $p = 0.5453$, unpaired two-tailed t -test) of light-stimulated vs. control (dark) groups during the experiment after subtracting baseline level. **(K)** Representative intracameral tonometry of control (dark, top) and light-stimulated groups (middle) following intravitreal tracer injection, in addition to a high temporal resolution view of light-stimulated group (bottom, yellow bars represent individual light stimuli). **(L)** Spectral analysis of intracameral IOP recording shows no significant peak around the 1 Hz frequency band used for light stimulation ($n = 5-6$, n.s. $p = 0.5368$, Mann-Whitney test).

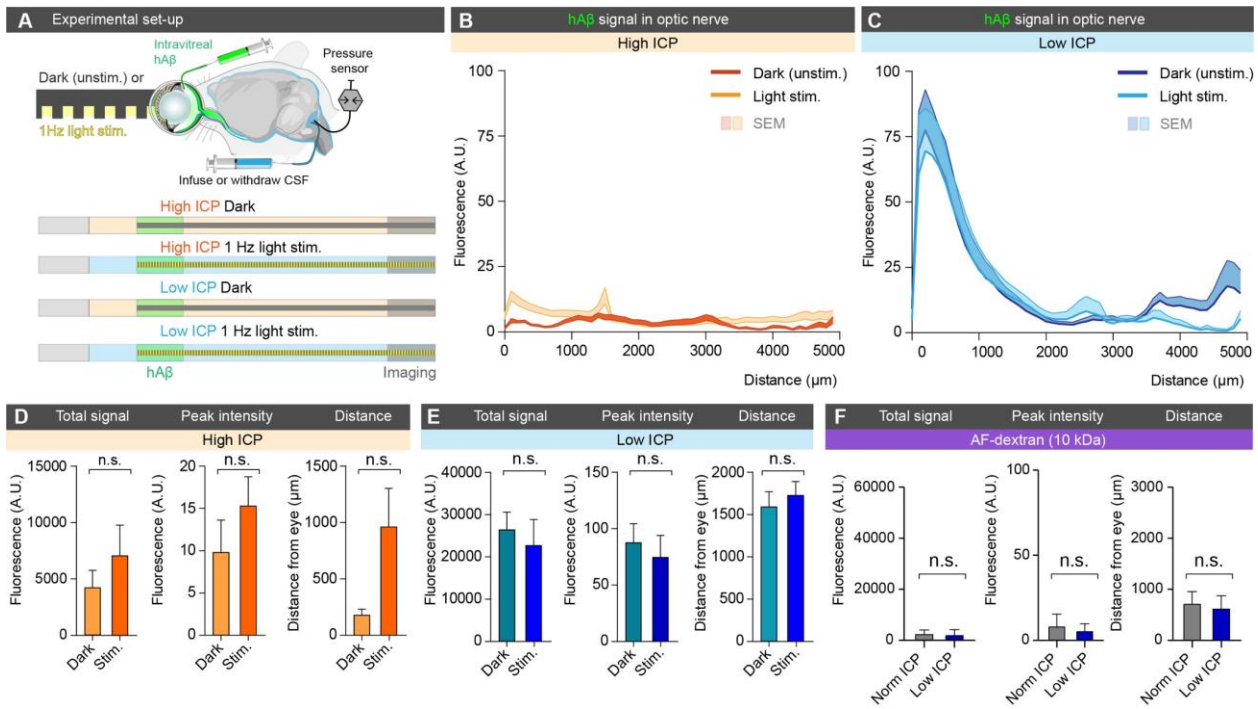


Fig. S6. Influence of the translaminal pressure difference on stimulated and unstimulated tracer movement. (A) Schematic of experimental design used for intravitreal injection with concurrent manipulation of intracranial pressure (ICP) and exposure to 1 Hz light stimulation or dark (unstimulated). (B-C) Averaged fluorescent intensity profiles of hAβ tracer distribution along the optic nerve in unstimulated and 1 Hz light-stimulated groups under high and low ICP conditions ($n = 5-6$). (D-E) Total hAβ tracer signal, peak intensity, and distance of hAβ tracer transport in the optic nerve following intravitreal injection in either high ICP condition or low ICP condition ($n = 5-6$, n.s. $p = 0.104-0.627$, unpaired two-tailed t -test). (F) Total signal, peak signal, and distance travelled for intravitreal AF-dextran (10 kDa) in the setting of normal vs. low ICP ($n = 6-8$, n.s. $p = 0.6620$ for total, 0.4109 for peak, 0.7774 for distance, unpaired two-tailed t -test for distance and peak, Mann-Whitney test for total).

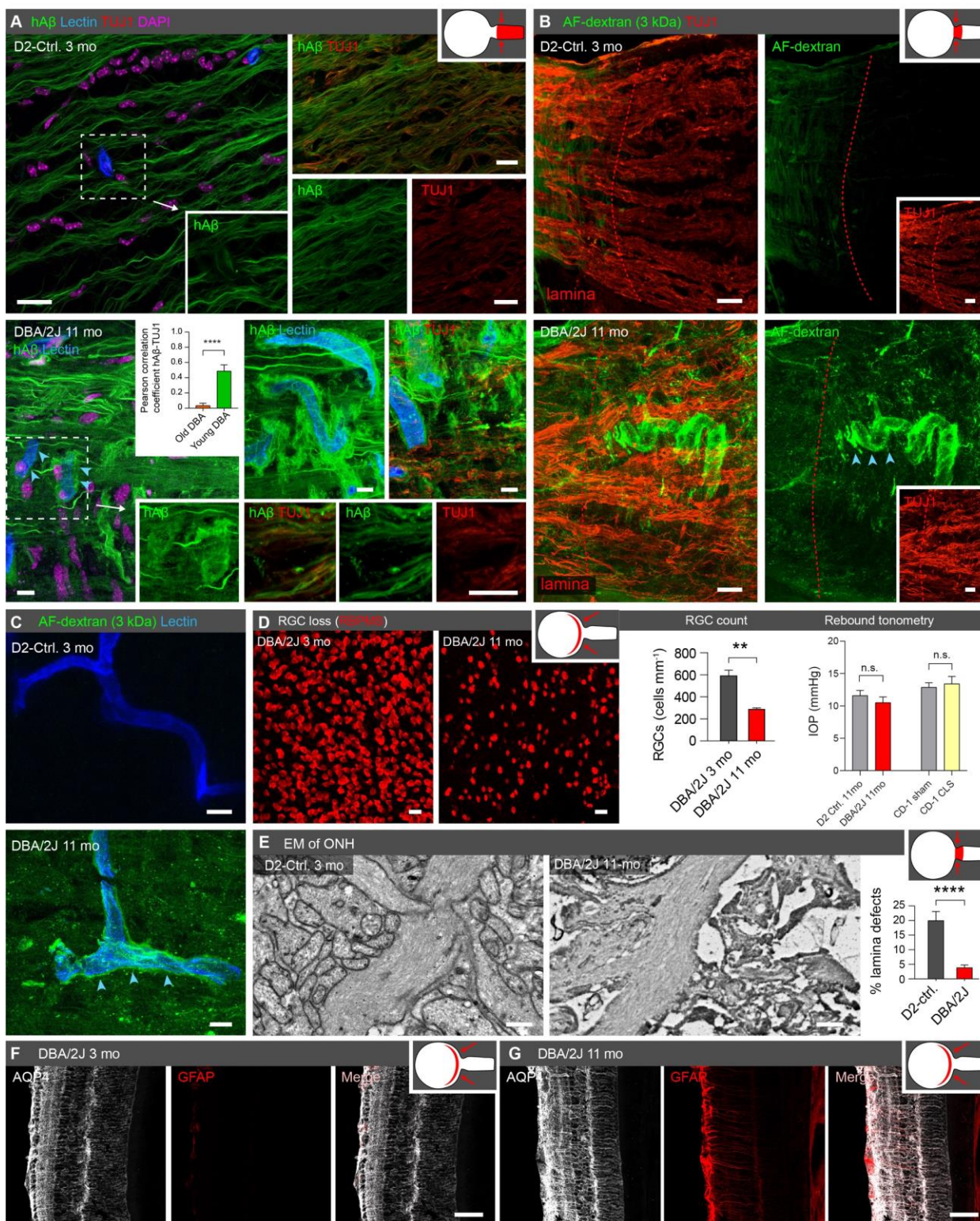


Fig. S7. Tracer efflux pattern in murine glaucoma model indicates leaky lamina that may allow bypass of intra-axonal transport via extracellular route. (A) Representative confocal images of the ipsilateral optic nerve following intravitreal hA β tracer injection from D2-control (top) and 11-month-old DBA/2J mouse

(bottom). (blue arrowheads: perivascular transport, scale: 20 μm). Bar graph shows Pearson correlation coefficient for TUJ1 and hA β labelling in young vs. old DBA mice ($n = 11-20$, **** $p < 0.0001$, Mann-Whitney test). **(B)** Confocal images of the optic nerve head stained for axonal marker TUJ1 after intravitreal injection of AF-dextran (3 kDa) in D2-control (top) and old DBA/2J mice (bottom). Red dotted line indicates the location of lamina blue arrowheads points to perivascular AF-dextran in old DBA/2J mice (scale: 20 μm). **(C)** Higher magnification confocal image of post laminar region of optic nerve following AF-dextran from control (top) or old DBA/2J mice (bottom). Blue arrowheads points to perivascular AF-dextran in old DBA/2J mice. (scale: 10 μm). **(D)** Left: Representative confocal images of retina flat-mount demonstrating a loss of RGCs in old DBA/2J mice compared to young DBA/2J animals (scale: 20 μm). Middle: Quantification of RGC number in young DBA/2J vs. old DBA/2J mice by counting RBPMS+ cell in retina flat-mount ($n = 9-10$, ** $p < 0.01$, n.s. $p = 0.436$ unpaired two-tailed t -test). Right: IOP in both glaucoma models compared to their controls at the time of experiment. ($n = 7-8$, n.s. $p = 0.3773$ for DBA, n.s. $p = 0.6870$ for CLS, unpaired 2-tailed t -test. CLS mice under isoflurane-induced anesthesia). **(E)** Left: Representative electron micrographs from the glial lamina region of young D2-control (top) and old DBA/2J mice (bottom) (scale: 0.5 μm) shown here without pseudo-coloring as compared to **Fig. 4I**. Right: Quantification of defects in the glial lamina taken as the percentage pixels out of the total area of the EM image $> 2\text{SD}$ above the average parenchymal pixel value, excluding blood-vessels ($n = 7-10$, **** $p < 0.0001$, unpaired two-tailed t -test). **(F-G)** Representative confocal retinal images stained for aquaporin-4 (AQP4, white) and glial fibrillary acidic protein (GFAP, red) comparing young and aged DBA/2J mice (scale: 50 μm).

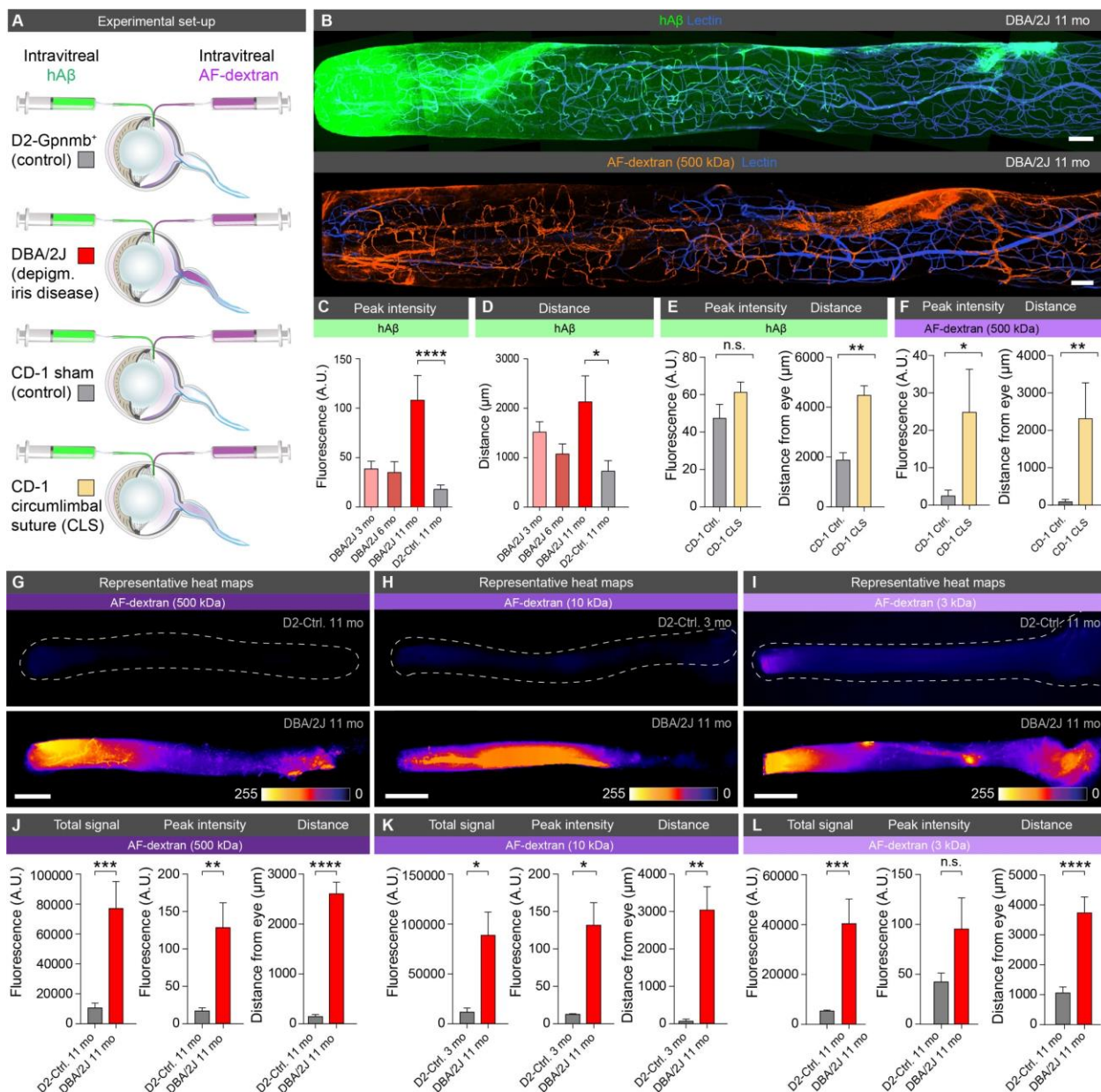


Fig. S8. Murine glaucoma models reveal defects in the lamina barrier allowing escape of large intraocular tracers. (A) Schematic of the experimental set-up for intravitreal injection of different size AF-dextran tracers (3, 10, 500 kDa) and hAβ tracer in DBA/2J and chronic circumlimbal suture (CLS) glaucoma models. (B) Representative confocal images of the ipsilateral optic nerve following intravitreal injection of hAβ tracer (top) and AF-dextran (bottom) in old DBA/2J mice (scale: 100 μm). (C-F) Peak intensity and distance of hAβ and AF-dextran (500 kDa) tracer transport in the optic nerve in 11-month-old DBA/2J, age-matched D2-control, as well as young and mid-age DBA/2J and CLS mice along with CD-1 controls ($n = 6-11$, $*p < 0.05$,

$**p < 0.01$, $****p < 0.0001$, n.s. $p = 0.1255$, Kruskal-Wallis test followed by Dunn's *post hoc* test or unpaired two-tailed *t*-test, or Mann-Whitney test). **(G-I)** Representative background-subtracted heat-maps of optic nerve following AF-dextran (3, 10, and 500 kDa) tracer injection in D2-control and old DBA/2J mice (scale: 500 μ m). **(J-L)** Total hA β tracer signal, peak intensity, and distance of AF-dextran tracer transport along the optic nerve for 500, 10, and 3 kDa AF-dextran ($n = 6-9$ [500 kDa groups], $n = 4-8$ [10 kDa groups], $n = 6-10$ [3 kDa groups], $*p < 0.05$, $**p < 0.01$, $***p < 0.001$, n.s. $p = 0.069$, unpaired two-tailed *t*-test).

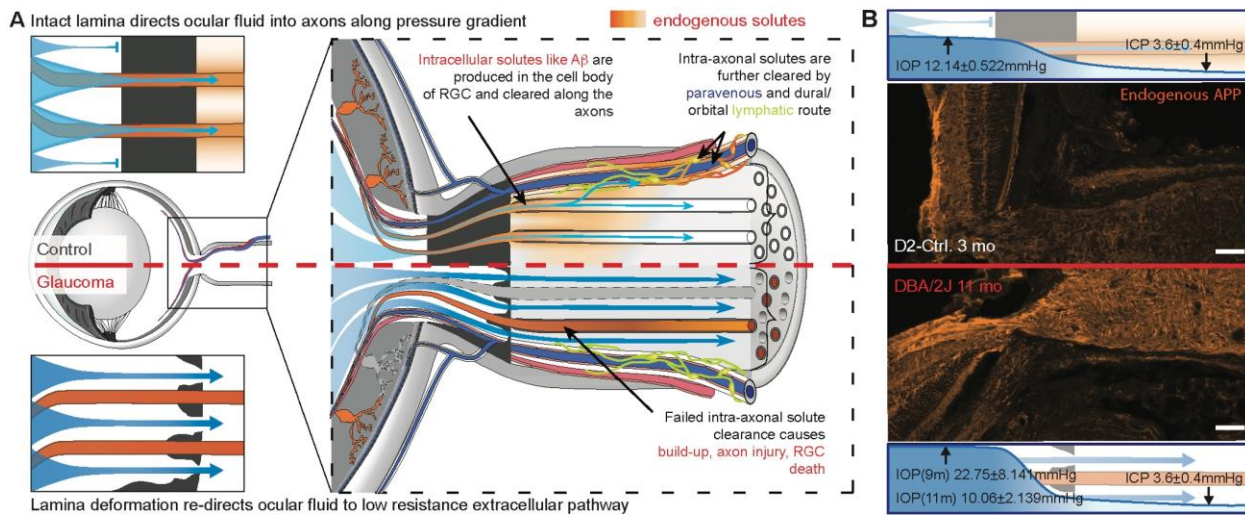


Fig. S9. Schematic model of the ocular glymphatic clearance system and its dysfunction in a murine model of glaucoma. (A) In control mice (top), IOP drives intraocular fluid (IOF, blue) into RGC axons prior to the glial cell barrier of lamina cribrosa (black). Intra-axonal transport of solutes (orange) across the lamina is accelerated by IOF uptake by RGC axons. After passing the glial lamina, hA β is released into the extracellular space, disperses into the perivenous space, and is eventually cleared by dural/orbital lymphatic vessels, where some tracer may also arrive from anterior and peri-papillary choroidal drainage paths. Insert illustrates how IOP in combination with the glial lamina barrier drives IOF into the unmyelinated RGC axons. In old DBA/2J mice (bottom), the barrier function of the glial lamina is lost, resulting in IOF passing directly into the extracellular space of the optic nerve via defects in the lamina, thus bypassing the intra-axonal compartment. The reduction of intra-axonal flow results in accumulation of potentially harmful solutes, such as A β (dark orange axons), and axonal degeneration (grey axons). Insert shows IOF bypassing the glial lamina through openings in the barrier. (B) Depicts immunolabeling of endogenous (mouse) amyloid precursor protein (APP) in young (top) and old (bottom) DBA mice (scale: 20 μ m). Above and below the immunohistogram are diagrams of how the translaminar gradient and lamina barrier differ between control and aged DBA/2J mice. DBA/2J mice IOP lowered at 11 months of age, which is the age we used them for experiment.

Table S1. Retinal cytokine assay comparing intravitreal hA β injection to vehicle.

Cytokine	Vehicle	Amyloid- β	<i>p</i> -value
Eotaxin	1.95 \pm 0.51	2.28 \pm 0.38	0.8147
G-CSF	0.40 \pm 0.09	0.43 \pm 0.04	0.9222
GM-CSF	2.73 \pm 0.09	2.60 \pm 0.03	0.2682
IFN- γ	0.27 \pm 0.02	0.27 \pm 0.02	0.9430
IL-1 α	26.21 \pm 3.28	31.42 \pm 5.63	0.7324
IL-1 β	4.64 \pm 0.23	4.89 \pm 0.61	0.9412
IL-2	15.36 \pm 0.81	14.68 \pm 2.14	0.9655
IL-3	0.35 \pm 0.01	0.35 \pm 0.01	0.9949
IL-4	0.48 \pm 0.01	0.48 \pm 0.01	0.9785
IL-5	0.39 \pm 0.01	0.39 \pm 0.003	0.9101
IL-6	1.31 \pm 0.18	0.92 \pm 0.19	0.2646
IL-7	0.64 \pm 0.16	0.45 \pm 0.12	0.6271
IL-9	18.63 \pm 1.52	18.87 \pm 1.38	0.5997
IL-10	2.83 \pm 0.15	3.00 \pm 0.41	0.9498
IL-12 (p40)	0.05 \pm 0.01	0.09 \pm 0.02	0.4405
IL-12 (p70)	2.12 \pm 0.11	2.03 \pm 0.14	0.8350
IL-13	1.57 \pm 0.05	1.54 \pm 0.04	0.9821
IL-15	3.56 \pm 0.40	3.39 \pm 0.25	0.9343
IL-17	0.50 \pm 0.02	0.51 \pm 0.03	0.9576
IP-10 (CXCL10)	1.49 \pm 0.22	2.42 \pm 0.40	0.2877
KC (CXCL1)	6.52 \pm 0.32	6.54 \pm 0.64	0.9999
LIF	0.35 \pm 0.01	0.39 \pm 0.02	0.0957
LIX (CXCL5)	0.12 \pm 0.01	0.12 \pm 0.004	0.9960
MCP-1 (CCL2)	4.22 \pm 0.63	5.02 \pm 0.88	0.6815
M-CSF	0.55 \pm 0.05	0.58 \pm 0.06	0.9645
MIG (CXCL9)	8.91 \pm 1.61	11.47 \pm 1.43	0.4758
MIP-1 α (CCL3)	5.49 \pm 1.23	5.93 \pm 2.33	0.9819
MIP-1 β (CCL4)	1.63 \pm 0.38	1.02 \pm 0.14	0.1897
MIP-2 (CXCL2)	16.51 \pm 3.00	14.5 \pm 1.70	0.8264
RANTES (CCL5)	0.61 \pm 0.06	0.62 \pm 0.03	0.9980
TNF α	0.29 \pm 0.02	0.32 \pm 0.02	0.4132
VEGF	0.64 \pm 0.04	0.64 \pm 0.09	0.9953

Table S2. Comparison of the controls for the DBA/2J strain.

Measurements	Values (mean \pm SD)		<i>p</i> -value
	C57BL/6J	<i>Gpnmb</i> ⁺ /SjJ (D2-control)	
young unstim total signal	5463 \pm 4843.8 (A.U.)	11753 \pm 6001.2 (A.U.)	0.14
young stim total signal	22889 \pm 9173.3 (A.U.)	23621 \pm 14946.6 (A.U.)	0.97
young unstim distance	890 \pm 354.0 (μ m)	1208 \pm 327.5 (μ m)	0.15
young stim distance	2020 \pm 775.4 (μ m)	1205 \pm 402.7 (μ m)	0.09
young unstim peak	28 \pm 11.7 (A.U.)	47 \pm 23.1(A.U.)	0.24
young stim peak	76 \pm 27.4 (A.U.)	95 \pm 59.2 (A.U.)	0.74
young IOP	13.0 \pm 3.57 (mmHg)	11 \pm 3.1 (mmHg)	0.16
old unstim total signal	9670 \pm 4911.8 (A.U.)	6830 \pm 5069.6 (A.U.)	0.36
old unstim distance	472 \pm 114.3 (μ m)	402 \pm 396.4 (μ m)	0.70
old unstim peak	18 \pm 7.0 (A.U.)	21 \pm 11.1 (A.U.)	0.50
old IOP	13.3 \pm 3.58 (mmHg)	12 \pm 1.8 (mmHg)	0.11

Table S3. Tracers used and their routes of administration.

Tracer	Route
^3H -mannitol	Intra-arterial
$^{86}\text{Rb}^+$	Intra-arterial
Cadaverine, FITC-conjugated	Intra-arterial
Cadaverine, FITC-conjugated	Intravitreal
Cadaverine, FITC-conjugated	Supra-choroidal
Ovalbumin, FITC-conjugated	Supra-choroidal
hA β , HiLyte Fluor 488-conjugated	Intravitreal
3 kD dextran, Alexa Fluor 488-conjugated	Intravitreal
3 kD dextran, Alexa Fluor 555-conjugated	Intracisternal
3 kD dextran, Alexa Fluor 555-conjugated	Intravitreal
3 kD dextran, Alexa Fluor 647-conjugated	Intravitreal
10 kD dextran, Alexa Fluor 488-conjugated	Intravitreal
10 kD dextran, Alexa Fluor 555-conjugated	Intravitreal
10 kD dextran, Alexa Fluor 647-conjugated	Intravitreal
500 kD dextran, Alexa Fluor 488-conjugated	Intravitreal
500 kD dextran, Alexa Fluor 555-conjugated	Intravitreal
500 kD dextran, Alexa Fluor 647-conjugated	Intravitreal

Movie S1. Animation of the proposed mechanism for ocular glymphatic clearance in the healthy optic nerve and glaucoma. Top-left panel shows intraocular fluid (IOF, blue) propelling the translaminal transport of intra-axonal solutes (orange) along the ocular-cranial pressure gradient, which then is cleared by a perivenous and lymphatic route. Top-right panel demonstrates how the lamina barrier (dark grey) might guide IOF into unmyelinated retinal ganglion cell (RGC) axons at the level of the optic nerve head. Bottom-left panel shows how in glaucoma, defects in the lamina barrier could allow IOF (blue) to bypass the intra-axonal compartment and diffuse directly into the extracellular space of the retro-laminar optic nerve. The reduction in intra-axonal solute flow would be expected to cause an accumulation of neurotoxic compounds such as A β (dark orange). Bottom-right panel illustrates how lamina defects cause a redirection of IOF, so it is no longer driving directional intra-axonal flow, causing intra-axonal solute accumulation.